Physics of Plasmas ARTICLE scitation.org/journal/php

Laser-driven strong shocks with infrared lasers at intensity of 10^{16} W/cm^2

Cite as: Phys. Plasmas **26**, 112708 (2019); doi: 10.1063/1.5119697
Submitted: 12 July 2019 · Accepted: 8 October 2019 ·
Published Online: 19 November 2019 · Publisher error corrected 26 November 2019

L. Antonelli,[1] J. Trela,[2] F. Barbato,[2] G. Boutoux,[2] Ph. Nicolaï,[2] D. Batani,[2] V. Tikhonchuk,[2,3] D. Mancelli,[2,4] A. Tentori,[2] S. Atzeni,[5] A. Schiavi,[5] F. Baffigi,[6] G. Cristoforetti,[6] S. Viciani,[6] L. A. Gizzi,[6] M. Smid,[3,7] O. Renner,[3,8] J. Dostal,[3,8] R. Dudzak,[3] L. Juha,[3,8] and M. Krus[8]

AFFILIATIONS

[1]York Plasma Institute, Department of Physics, University of York, York YO10 5DQ, United Kingdom
[2]Université de Bordeaux, CNRS, CEA, CELIA (Centre Lasers Intenses et Applications), UMR 5107, F-33405 Talence, France
[3]Institute of Physics and ELI Beamlines, Czech Academy of Sciences, Czech Republic
[4]Donostia International Physics Center (DIPC), Donostia/San Sebastian, Basque Country, Spain
[5]Dipartimento SBAI, Università degli Studi di Roma "La Sapienza," Via Antonio Scarpa 14, 00161 Roma, Italy
[6]Intense Laser Irradiation Laboratory, INO CNR (National Council of Research), Pisa, Italy
[7]Helmholtz-Zentrum Dresden-Rosendorf, Dresden, Germany
[8]Institute of Plasma Physics, Czech Academy of Sciences, Prague, Czech Republic

ABSTRACT

We present the results of an experiment on laser-driven shock waves performed at the Prague Asterix Laser system (PALS), where the fundamental frequency of the laser (1315 nm) is used to launch a strong shock in planar geometry. The experiment aims to characterize both shock waves and hot electrons generated at intensities of $\simeq 10^{16}$ W/cm^2. It is shown that, in these interaction conditions, hydrodynamics is strongly impacted by noncollisional mechanisms, and the role of the hot electrons, generated by parametric instabilities, is essential in determining shock dynamics.

I. INTRODUCTION

The shock ignition approach to inertial confinement fusion (SI)[1] presents several advantages compared to the standard central ignition approach,[2] such as a lower implosion velocity in the compression phase, which makes SI less sensitive to hydrodynamic instabilities, and a lower amount of energy needed to achieve ignition.[3,4] In the SI scheme, ignition is triggered by a strong shock (>300 Mbar) launched by a laser spike of duration a few hundred picoseconds close to the end of the compression phase, with intensity between 10^{15} and 10^{16} W/cm^2. Interaction of the laser spike is expected to be strongly affected by parametric instabilities such as Stimulated Brillouin Scattering (SBS), Stimulated Raman Scattering (SRS), and Two Plasmon Decay (TPD), which reduce the laser energy coupled with the target and can also produce suprathermal electrons.[5,6]

Several works have pointed out the essential role of such hot electrons (HEs) not only toward target preheating (a well-known effect in inertial fusion research)[7] but also in the process of shock generation and in determining shock dynamics.[8,9] It appears that if the energy of HEs is not too high, they could actually improve the laser-plasma coupling and increase the shock strength, while at the same time, they would not be able to penetrate deeply into the target and preheat the fuel.[8,10] Therefore, experiments have recently addressed the study of HE, parametric instabilities, and shock generation in the SI interaction regime. These include experiments done at OMEGA[11] in planar[12] and spherical geometries,[13–15] at LIL,[16] and at the Prague Asterix Laser system (PALS).[17,18] All of them made use of UV laser light, which is expected to result in a stronger coupling with denser plasma regions. The use of short wavelength laser light is essential for compressing inertial fusion targets because it guarantees a better hydrodynamics efficiency and a lower level of parametric instabilities. However, assuming that HEs have a beneficial effect for the generation of the final shock, it could be possible to think about mixed irradiation schemes where compression is performed at 3ω, and the final spike is realized at 1ω or 2ω. The advantage of using longer wavelength radiation is a lower level of damage to the optics for beam transport and the availability of larger energy. For example, at PALS,[19] the laser can routinely deliver 300 J in the third harmonic ($\lambda_0 = 438$ nm) but up to 700 J in the first harmonic ($\lambda_0 = 1.315\ \mu$m). Using phase plates to produce a uniform focal spot of 100 μm, the full width at half maximum (FWHM) provides an intensity of $\approx 1.5 \times 10^{16}$ W cm^{-2} on the target. If we consider the irradiance $I\lambda^2$, which is the physical quantity governing the onset of parametric instabilities, we reach $I\lambda^2 \approx 3 \times 10^{16}$ W μm^2 cm^{-2}, an order of magnitude higher compared to the third harmonic.

Such nonlinear interaction conditions may result in stronger SRS and TPD and consequently larger HE production, which should strongly affect shock dynamics. In addition, studying parametric instabilities and HE generation at high intensity and longer wavelengths will allow for a better understanding of the physical processes that take place and for retrieving quantitative information on thresholds and conversion efficiencies. Such information is essential for developing advanced numerical models and validating them.[10]

II. EXPERIMENTAL SETUP

Streaked-optical-pyrometry (SOP) was used to characterize dynamics of the shock waves, while focusing spectroscopy with spatial resolution (FSSR) and spherical crystal imaging (SCI) were used to characterize K_α emission generated by interaction of hot electrons[20] with tracer layers buried in the target. Parametric instabilities were studied by collecting light backscattered within the cone of the focusing lens and characterizing it by time integrated optical spectroscopy (OS) and calorimetry (Cal).[21,22] Bremsstrahlung emission was recorded using a bremsstrahlung cannon placed in front of the target (BC). A sketch of the experimental setup is shown in Fig. 1.

In this work, we focus on hydrodynamics and hot electron effects by analyzing SOP results through comparison with numerical simulations. Other diagnostics provided complementary information on laser-plasma interaction, which reinforces the proposed interpretation of the experiment and allows constraining simulation parameters. For some of them, the detailed analysis is developed in an associated article.[23]

PALS is a single beam laser delivering 700 J at a fundamental wavelength ($\lambda = 1.315\,\mu$m) in an $\sim$300 ps, full width half maximum (FWHM), Gaussian pulse. The beam was smoothed with a Random Phase Plate (RPP) providing a Gaussian focal spot of $\sim$100 μm (FWHM). The RPP diameter was 30 cm, and its focal length was 60 cm, leading to an f/#2 optical system. By performing accurate calorimetric measurements, we determined that only $\sim$50% of the nominal energy was contained in the 100 μm spot. Therefore, the effective laser energy inside the focal spot was 350 J. Figure 2 shows laser power as a function of time (right) and intensity distribution as a function of radius (left). Solid lines are horizontal and vertical line-outs of a time integrated image of the laser focal spot. The dashed line represents the smoothed profile used in simulations. The peak power of 1.10 TW results in a peak intensity on axis of 0.97×10^{16}W/cm^2 and in an interaction parameter $I\lambda^2 = 1.68 \times 10^{16}$ W μm^2 cm^{-2}, which is largely above the threshold for laser plasma instabilities. Hence, a significant amount of hot electrons is expected to be produced. The PALS beam was used to irradiate two-layer targets with a front layer of Polystyrene (CH) of variable thicknesses, ranging from 10 μm to 180 μm, followed by 5 μm of Titanium. The targets were embedded into an aluminum washer, and the inner diameter was 2 mm. The use of different plastic thicknesses allowed us to obtain information on both shock waves and HE heating.

III. EXPERIMENTAL RESULTS

A. X-ray measurements

Figure 3 shows a typical 2D-resolved image of the Ti K_α emission produced by hot electron interaction with a target (in this case, a 5-μm Ti layer covered by 10 μm of plastic). The elliptical shape of the emitting area corresponds to the oblique line of sight of the imager observing the target surface at an angle of about 45°. The measurement of the number of photons emitted by Titanium at this energy gives information on the flux of hot electrons. This flux depends on the thickness of the CH layer. Taking, for example, targets with 50 μm of CH, it can be found that only hot electrons with energies of $\geq$50 keV reach the

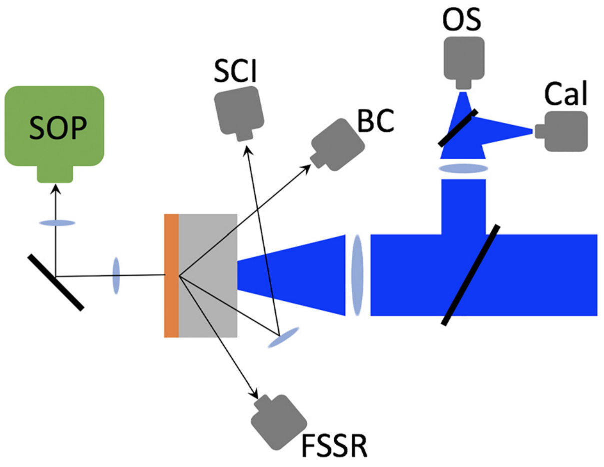

FIG. 1. Experimental setup.

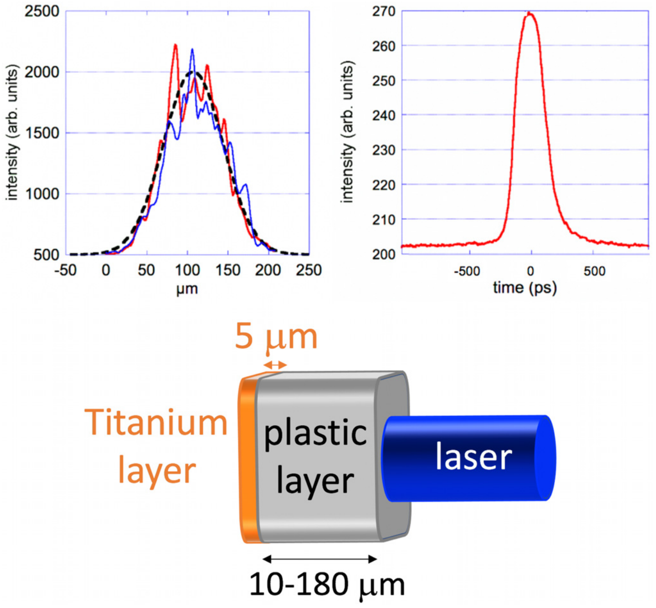

FIG. 2. (top-left) PALS laser focal spot (see the text) and (top-right) laser power as a function of time for a total energy of 700 J. Target scheme (bottom).

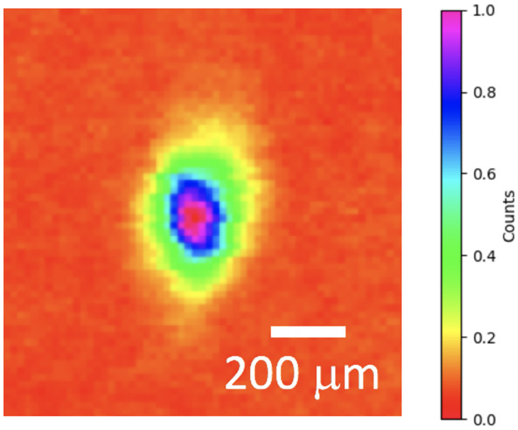

FIG. 3. Distribution of K_α emission from the 1ω-irradiated 5-μm-Ti foil covered by 10 μm of plastic, visualized by monochromatic imaging.

titanium layer. For targets with a thicker CH layer, this cut-off energy increases, which results in a reduction of hot electrons reaching the Ti layer and therefore a lower K_α signal. However, we observed the K_α signal even for the largest plastic thickness, implying the presence of a HE component at high energy. Figure 4 presents the analysis of the K_α signal as a function of the thickness of the CH layer. Squares represent the measured average fluxes at each thickness (these data refer to FSSR; however, data from the SCI provide similar results), while spheres represent simulations of hot electron fluxes. The analysis has been performed with the Monte Carlo code GEANT4[24] simulating propagation of hot electrons and the K-shell emission inside the studied target. The K-shell ionization cross sections were provided by the PENELOPE physics library.[25] The Monte Carlo simulation, which best-fits the experimental data, uses two Maxwellian hot electron populations—a dominant one with the temperature of $\simeq 40 \pm 5$ keV and a hotter one with the temperature of $\simeq 85$ keV $\pm$ 5 keV. In agreement with known scaling laws (and with the results of Ref. 23), we attribute the first component to hot electrons produced by SRS and the second one to TPD. The total conversion efficiency from the laser to hot electrons is $\eta = 5.3 \pm 0.58\%$, distributed as 2/3 and 1/3 for SRS and TPD, respectively. Note that, in previous campaigns at PALS, using 300 J energy at the third harmonic ($\lambda_0 = 438$ nm), the measured conversion efficiency was below 1% with the hot electron temperature of 25 ± 7.5 keV.[9,10]

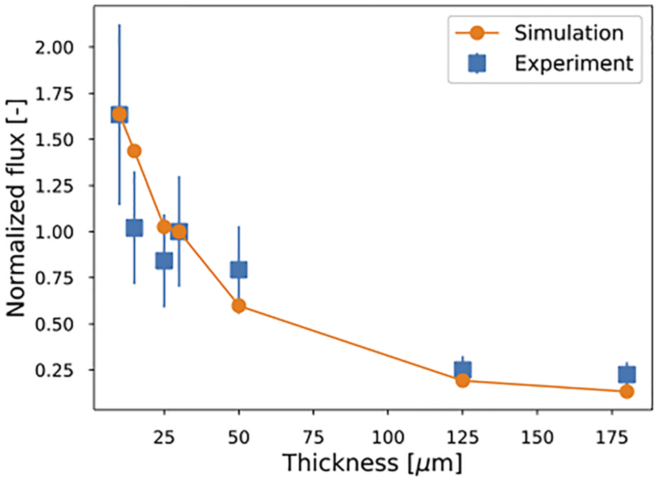

FIG. 4. Integrated K_α emission vs plastic thickness obtained using the FSSR spectrometer. Experimental points are averaged over several shots. Simulation points include the contribution of two Maxwellian hot electron populations, a dominant one with a temperature of $\simeq 40 \pm 5$ keV and a hotter distribution with a temperature of $\simeq 85 \pm 5$ keV.

B. Bremsstrahlung cannon

A bremsstrahlung cannon (BC) provides information on the high-energy photon distribution and hence indirectly allows us to estimate the hot electron energy distribution. The typical results from this diagnostic are shown in Fig. 5.

Monte Carlo simulations have been used in two steps to infer hot electron temperature. First, the BC structure has been fully simulated to obtain, at the entrance, the photon spectrum yielding signals in each image plate. In a second step, the MC code has been run to find the electron population, leading to the photon spectrum at the position of diagnostic. The best results were systematically obtained using a Maxwellian distribution at an electron temperature of 45 ± 10 keV.

C. Streaked optical pyrometer

Information on the shock wave dynamics was obtained thanks to Streaked Optical Pyrometry (SOP) that measures the breakout time of

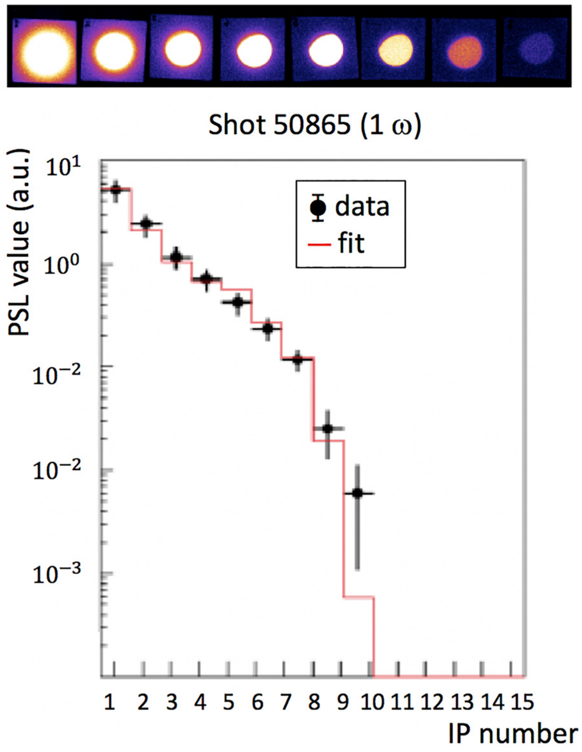

FIG. 5. Raw data from BC (each circle corresponds to a different IP) and fit related to a photon spectrum at the entrance of the diagnostic.

the shock at the rear side of the target. The target is imaged on the slit of a streak camera that records the self-emission of the Titanium layer in the visible range of the electromagnetic spectrum. Figure 6 presents the SOP signal for three representative plastic thicknesses: 15, 50, and 125 μm. Line-outs of the SOP signal as a function of time are also displayed. The peak of emission observed at early times is due to preheating of the rear surface by hot electrons reaching the Titanium layer after crossing the plastic layer. Practically, it occurs at the time of the maximum laser intensity. Due to such significant preheating, the target rear side expands rapidly, cooling down, which implies a rapid reduction of the emitted thermal radiation. For 50 μm and 125 μm plastic thicknesses, a second peak of emission is clearly visible. It is induced by the shock produced at the front side of the target that crosses the whole target, heating and compressing it and finally reaching the rear side. For the target with 125 μm of CH, the delay between the peak due to hot electrons and the signal rising due to shock breakout is 4.1 ± 0.2 ns. For the target with 50 μm, this delay is 1.0 ± 0.1 ns. For the target with 15 μm of CH, there is no signal rise, and so the delay cannot be defined. This does not mean that there is no shock but simply that the hot electron heating dominates the shock heating, hiding its arrival at the rear side. The signal due to hot electron preheating decreases with the plastic thickness, as expected. This is due to the fact that when the propagation thickness increases, fewer electrons arrive at the Ti layer, reducing its heating. At the same time, the signal corresponding to shock breakout also decreases because for larger propagation distances, the shock pressure reduces. However, for large thicknesses, although reduced, it becomes larger than the initial peak due to hot electrons.

D. Parametric instabilities

The impact of noncollisional processes in this interaction regime, giving rise to HEs, is confirmed by spectroscopic and calorimetric measurements of scattered light. In our setup, due to the low spectral

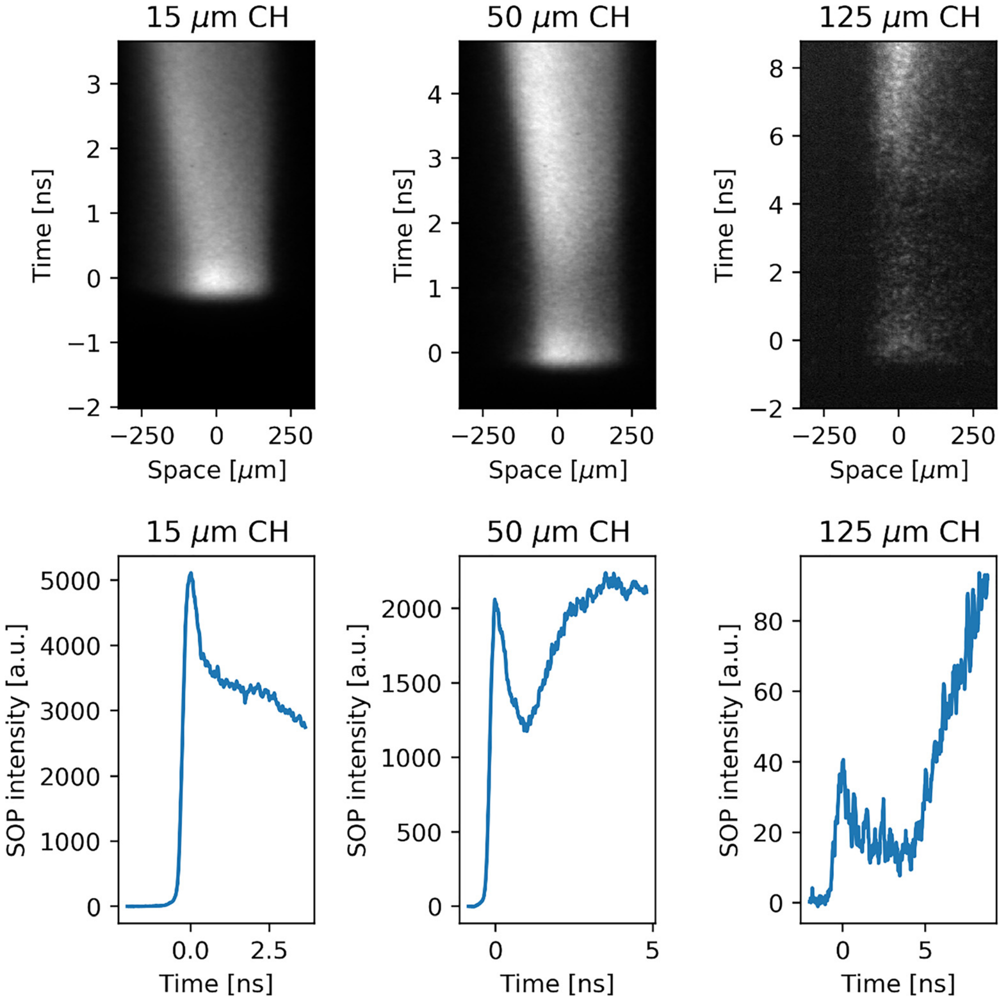

FIG. 6. Streak images of rear side emission for different thicknesses of the CH layer (top row) and corresponding line-out as a function of time (bottom row). The time t = 0 is defined by the peak of the emission due to the electrons. For the target with a 125 μm thick CH layer, the signal rises at t = 4.1 ± 0.2 ns due to shock breakout. For the target with 50 μm of CH, this rises at t = 1.0 ± 0.1 ns. For the target with 15 μm of CH, the shock breakout time cannot be precisely measured.

resolution of the optical diagnostics, we were not able to distinguish SBS from laser light simply reflected from the target. The reflectivity due to SRS, in the lens cone, was 0.6–4% of laser energy. Comparing such results to our previous measurements performed at 3ω,[21,22] we observe a large increase in SRS, which can be explained by the increase in the irradiance parameter ($I\lambda^2$), which determines the convective gain in the resonance region. The measured increase in SRS is consistent with the rise in the hot electron signal, suggesting that the main HE component is generated by SRS. This is further confirmed by the spectral characterization of SRS back reflectivity, showing a maximum in the spectral range of 2400–2450 nm,[23] implying that SRS is preferentially emitted at densities of 0.17–0.19 n_c. In this case, assuming a background plasma temperature to be ~4 keV (as extracted from simulations and as expected from simple scaling laws), we can estimate that the energy of electrons accelerated by the plasma waves produced by SRS is ~40 keV, in fair agreement with our experimental findings.

IV. DISCUSSION

E. The numerical tool

Numerical simulations of the experiment were performed with the hydrodynamic code CHIC,[26] which includes a model[10] accounting nonlinear laser-plasma interaction (LPI), the generation of hot electrons, and their propagation into the plasma. The description of the laser propagation is based on the Paraxial Complex Geometrical Optics (PCGO): the laser beam is described by a bunch of thick Gaussian rays. Unlike models based on ray tracing, the PGCO model calculates laser intensity in plasma and allows computing parametric instabilities and subsequent hot electron production. The electron transport model is described in the continuous slowing down approximation considering electron-ion and electron-electron collisions. The hot electrons are described by an exponential distribution function in energy that is logarithmically discretized in a series of monoenergetic beamlets. This multigroup model for HE beam transport in plasmas has been validated by comparison with a reference code.[27] The free parameters defining the hot electron source are initial energy flux, mean temperature, angular distribution, and direction. These parameters are determined from laser and plasma characteristics, thus coupling parametric instabilities and hot electron sources. In CHIC, they are computed using scaling laws obtained from extensive PIC simulations or experimental data.[10] For TPD HE, flux (W/cm^2) and temperature (keV) are defined as

$$F^{TPD} = 2.6 \times 10^{-2} I\left\{1 - \exp\left[-\left(\xi^{TPD} - 1\right)^{1/2}\right]\right\}, \qquad (1)$$

$$T^{TPD} = 15.5 + 17.7\xi^{TPD}, \qquad (2)$$

where $\xi^{TPD} = I/I^{TPD}$ is the ratio of the local intensity to the threshold intensity $I^{TPD} = 8.2T_{keV}/(L_{\mu m}\lambda_{\mu m})$ PW/cm^2, with $L_{\mu m}$ being the density scale length in μm. The electron plasma waves are excited by TPD in a broad range of directions within the cone ±45° with respect to the pump. Multiplicity of configurations for the pump and daughter waves produces a uniform hot electron emission in the ±45° cone with respect to the PCGO ray direction.

The energy of hot electrons produced by SRS is linked to the phase velocity of the electron plasma wave at the point of resonance. It is supposed that the hot electrons are produced at the density of $n_e = 0.2n_c$, and their temperature reads $T^{SRS} = 34 + 1.5T_{\mathrm{keV}}$.[10] The hot electron flux reads

$$F^{SRS} = 12.5 \times 10^{-2} I\left\{1 - \exp\left[-\left(\xi^{1/3} - 1\right)\right]\right\} \mathrm{W/cm^2}, \qquad (3)$$

where $\xi = I/I^{SRS}$ is the ratio of the local intensity to the threshold intensity. The threshold intensity can be calculated using the absolute or convective threshold formulas, $I^{SRS}_{abs} = 99.5/(L^2_{\mu m}\lambda_{\mu m})^{2/3}$ PW/cm^2 or $I^{SRS}_{conv} = 220/\left(L_{\mu m}\lambda_{\mu m}\sqrt{1 - n_e/n_c}\right)$ PW/cm^2, respectively. From experimental observations, it is known that SRS electrons are more directional than TPD electrons relative to the laser direction. In CHIC simulations, it is assumed that SRS electrons propagate in the laser beam direction. The model describing coupling between the laser beam, plasma dynamics, hot electron generation, and propagation has been used to better simulate experiments in the intensity range of 10^{15}–10^{16} W/cm^2 with $\lambda = 351$ nm.[10] Nevertheless, for longer laser wavelengths, the scaling laws used to define the hot electron sources from TPD and SRS have to be validated/tuned by comparison with experimental measurements.

F. Simulation without the hot electron

We performed CHIC simulations using the PCGO description of the laser beam, including or not the hot electron effects on hydrodynamics. The three plastic thicknesses, 15, 50, and 125 μm, have been tested. All the simulations share a common time scale. The zero time corresponds to the beginning of the laser pulse and differs from experimental zero time used in Figs. 2 and 6 defined at the maximum laser intensity. Comparisons between experiment and simulation concern the delay time between emission induced by hot electrons and emission induced by the shock breakout and so are independent of the choice of zero time. A focus is made on the interpretation of the thickest CH layer, characterized by a longer distance traveled by the shock wave. Figure 7 presents the results from the simulation without hot electrons. In this simulation, only 9.3% of the laser energy has been absorbed through inverse Bremsstrahlung. This low absorption is due to the short pulse, long wavelength, and high intensity of the laser pulse. 2D maps of pressure and density 800 ps after the beginning of the simulation show a well-defined shock front with a pressure of ~12 Mbar. The maximum pressure, 14–15 Mbar, is reached just after the peak of laser intensity. This relatively low pressure, for a laser intensity of ~10^{16} W/cm^2, can be explained by two main reasons. First, at the first harmonic, laser-plasma coupling is weak. The laser absorption is less than 10% and takes place at a density of 6.5×10^{20}cm^{-3}. Locally, plasma temperature is high but pressure due to a low density is small. The second reason is a small focal spot diameter of ~100 μm. Lateral losses are important and strongly reduce the pressure. A one dimensional simulation or a spherical geometry leads to higher pressure. However, this pressure is large enough to compress the plastic up to 3.6 times its initial density. Pressure and density maps as a function of time and space show that the shock propagates through the two layers and breaks out at the rear side of the target 4.45 ns after the beginning of the simulation.

Synthetic SOP images have been produced by looking at the total radiation escaping from the target rear side in the range of 1–4 eV accounting for the spectral acceptance of the SOP diagnostic (streak camera sensitivity plus transport optics). In addition, we have taken into account the spatial (80 μm) and temporal resolution (80 ps) of the diagnostics.

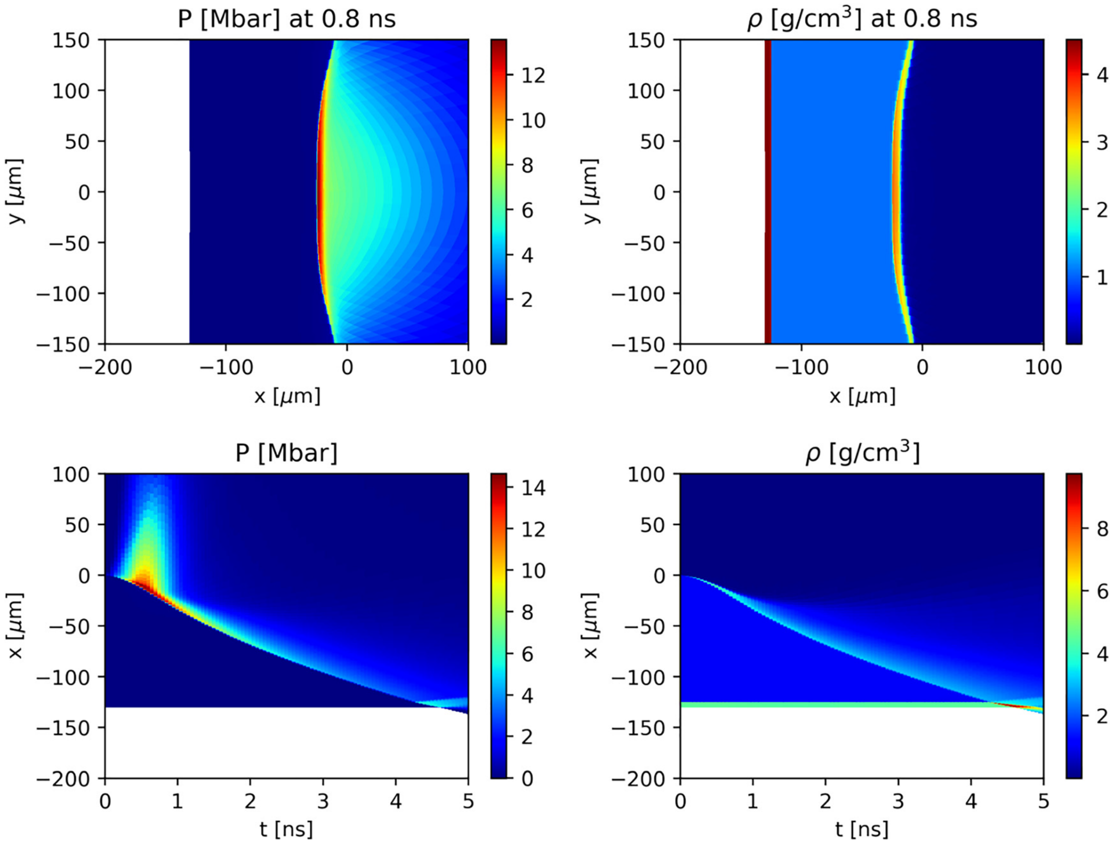

FIG. 7. Simulation without hot electrons. 2D map of pressure at 800 ps (top left), 2D map of density at 800 ps (top right). Pressure as a function of time and space (bottom left). Density as a function of time and space (bottom right).

As expected, in Fig. 8, only heating induced by the shock appears on the SOP signal, and the first emission induced by hot electrons is not reproduced by this simulation. Note that the X-ray emission produced by the laser-plastic interaction is not strong enough to heat the Ti layer and to be registered on the SOP signal.

At this step, an important remark has to be done concerning simulations and comparisons with experimental data. The CHIC code is a two dimensional hydro-code. Two geometries can be used: slab or cylindrical. The latter may be very close to 3D simulation in a case of cylindrical laser beam illuminating a target perpendicularly to the target surface. This geometry correctly represents the laser in terms of intensity, power, and energy. In planar geometry, the focal spot is a stripe with an intensity distribution, which is correct in one direction but invariant in the other one. To keep the same laser intensity on the target, the laser power has to be modified. For short hydrodynamic simulations or large focal spot dimension, both geometries lead to the same results. In this PALS experiment, the laser focal spot size was only 100 μm at FWHM, the pulse duration was short, and the shock was traveling distances longer than 100 μm during several nanoseconds. The geometry effect on shock propagation without hot electrons can be tested for the different plastic thicknesses using the model based on ray tracing (the PCGO model is for the moment implemented in planar geometry only). For the thickest layer, 125 μm, the shock breakouts 600 ps later in the cylindrical case compared to that in the slab one. This is mainly due to different lateral losses during the shock creation and its propagation. Indeed, if in the cylindrical case, these losses are correctly calculated, in slab geometry, the invariance by translation in one direction reduces losses, leading to a higher pressure and finally to a faster shock. This effect is smaller for thinner targets. For the 50 μm thickness, the delay between the two geometries is only 50 ps, and no difference is observed for the 15 μm thickness.

G. Simulation with hot electrons

When simulating the case of the 125 μm target with hot electrons, we have assumed that the difference between planar and axisymmetric geometries still results in a shock breakout difference of 600 ps. All the following simulations have been performed in slab geometry.

Figure 9 presents hydrodynamics with hot electrons. Both SRS and TPD electrons have been considered. The temperatures and conversion efficiencies of the electron sources are given by Eqs. (1) and (3). For the SRS electrons, the time averaged temperature and conversion efficiency are 39 keV and 9.2%, respectively. We used for this run the absolute intensity threshold. For the TPD electrons, these parameters are 83 keV and 1.9%. The SRS hot electrons have no initial divergence, while the TPD hot electrons have a ±45° divergence.

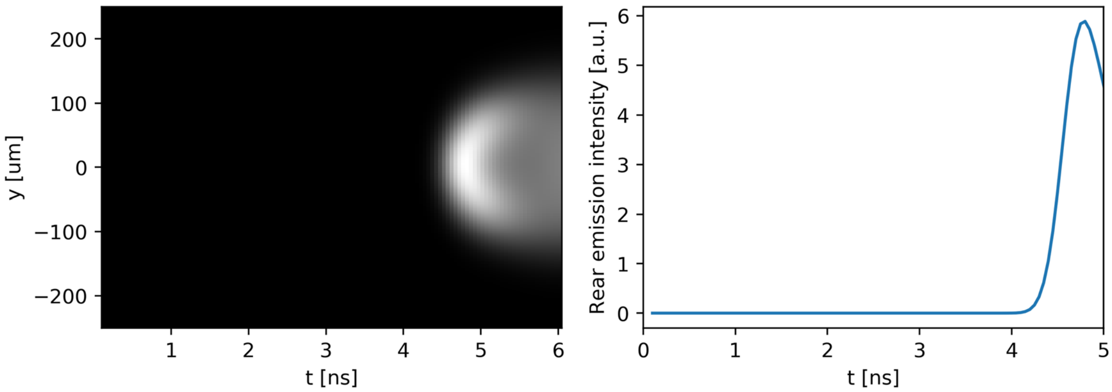

FIG. 8. Synthetic SOP image obtained by postprocessing the results of CHIC simulations, without HE (left) and line-out of this results along the axis $y = 0$ (right).

Additionally, 8.2% of the laser energy is absorbed through inverse Bremsstrahlung. Hence, collisional absorption is smaller than absorption by parametric instabilities. 2D maps of pressure and density 800 ps after the beginning of the simulation (Fig. 9, top row) show the effects of hot electrons on hydrodynamics of the target. Hot electrons heat the target both upstream and downstream of the shock front. In the unshocked plastic, this heating increases the pressure up to a maximum value of about 110 Mbar. We must notice, however, that in this case, the pressure profile is not sharp, as the one obtained without hot electron, but is characterized by a slow spatial decay. In this simulation, because of a high upstream pressure, due to preheat, the shock wave compresses the plastic only by a factor of 1.15. The pressure increase due to the hot electron energy deposition also leads to expansion of the target from both sides. At the rear side, the heated

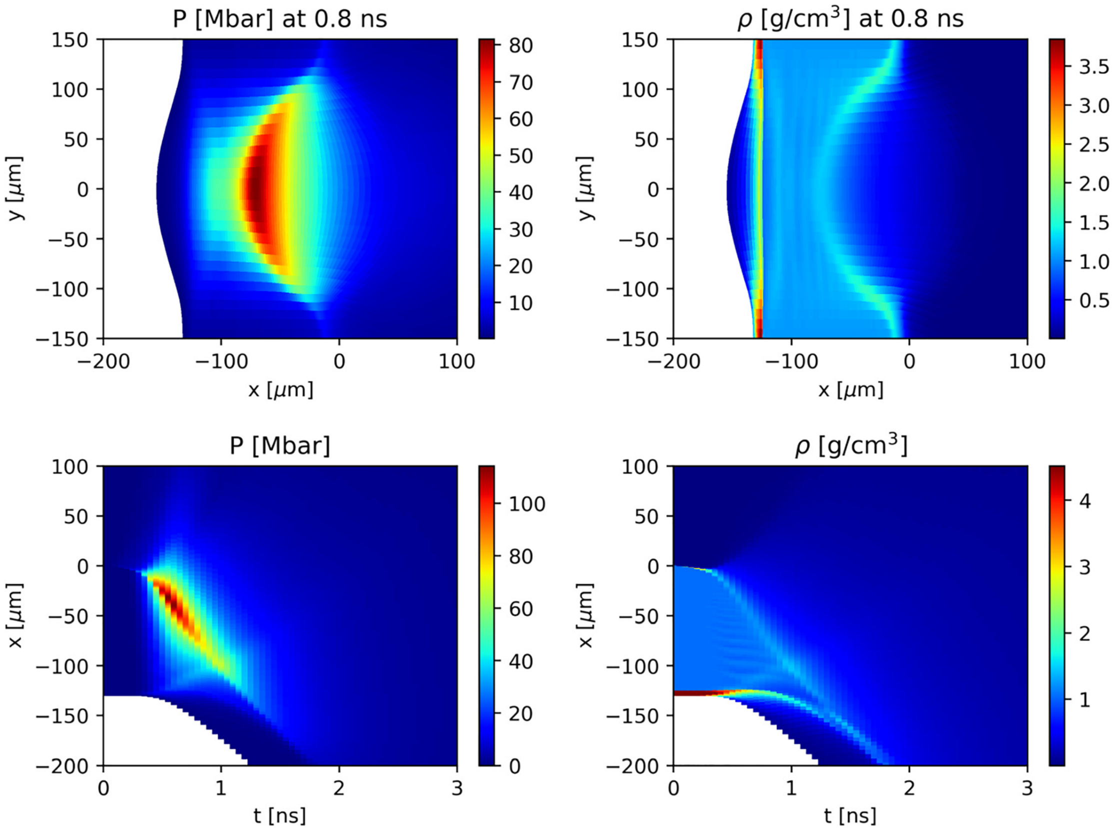

FIG. 9. Simulation with hot electrons. 2D map of pressure at 800 ps (top left). 2D map of density at 800 ps (top right). Pressure as a function of time and space (bottom left). Density as a function of time and space (bottom right).

Titanium layer expands into vacuum, creating a decreasing density gradient. Due to the directionality of the SRS hot electrons, this heating is localized close to the laser symmetry axis ($y = 0$). As a consequence, the shock front curvature is larger in the simulation with hot electrons. The pressure and density as a function of time and space (bottom row) show the dynamics of the target. The shock is faster in the simulation with hot electrons, and it reaches the Titanium layer at 1.6 ns, against 4.2 ns in the simulation without hot electrons. However, due to the large expansion of the Titanium layer, the breakout at the rear side of the target is not well defined. Figure 10 shows the synthetic SOP image obtained from this simulation. The emissivity of the rear side shows a behavior similar to the experiment. During laser matter interaction (before 800 ps), there is a peak of emissivity due to direct heating of the Titanium layer by the hot electrons. This signal then decreases with time as the layer expands and cools down. Then, the shock breaks out at the rear side of the target, leading to a second increase in the emissivity. In this simulation, the delay between the rising of the signal due to shock breakout and the peak of emission due to hot electrons is 1.6 ± 0.1 ns. Even considering 600 ps delay due to planar geometry, this is much shorter than the experimental delay (4.1 ± 0.2 ns). The disagreement between simulation and experiment is due to overestimation of the amount of hot electrons in the computation. Indeed, in this simulation, 9.2% of the laser energy is converted into SRS HE with a temperature of 39 keV. While the temperature is close to the measurements, the conversion efficiency is much larger in the simulation. In another simulation (not shown), the SRS intensity threshold has been changed from the absolute to the convective one. The latter intensity is higher, which leads to a smaller SRS electron flux but not small enough to reproduce experimental data. This inaccuracy in the scaling laws used to estimate HE source parameters is not surprising since these have mainly been determined from experiments and simulations at a shorter wavelength (typically 0.351 μm) and smaller $I\lambda^2$.

H. Effects of reduced hot electron fluxes

We therefore performed another set of simulations adjusting the HE flux and angular spreading with the goal of reproducing all experimental measurements (shock breakout time, hot electron temperature, and conversion efficiency). It is important to notice that the goal of this study is not to discuss in detail the origin of hot electrons but is to quantitatively characterize the hot electron amount and temperature required to reproduce their effects on hydrodynamics. This is of course more critical for SRS, which is the main source of hot electrons in our conditions. In particular, we compared the hot electron flux needed to reproduce experimental results to what predicated by scaling laws, either considering the intensity threshold for absolute SRS or that for convective SRS. Since the absolute SRS threshold is lower than the convective SRS threshold, it means that absolute SRS is triggered earlier in the laser pulse and acts for a longer time. Therefore, we get a higher hot electron flux from absolute SRS as compared to convective SRS. In both cases, we need to apply a reduction to the flux predicted by scaling laws in order to get the flux required to reproduce experimental results. This is a factor of about 4 if we consider absolute SRS and about 2 if we consider convective SRS. Physically, the reduction of hot electron fluxes needed for both SRS and TPD could be equivalent to modify the scaling laws for the fluxes by adding a wavelength dependence, but this reduction could also highlight a missing physical effect in simulations, for instance, related to the presence of strong magnetic fields close to the hot electron sources or other reasons. For both SRS and TPD sources, the temperatures and initial divergences have not been modified.

Figure 11 shows the effects of reduced hot electron fluxes on hydrodynamics. The conversion efficiencies of SRS and TPD are now 2.3% and 1.1%, respectively. Additionally, 9.3% of the laser energy has been absorbed through inverse Bremsstrahlung. 2D maps of pressure and density 800 ps after the beginning of the simulation (Fig. 11, top row) show that despite the flux reductions, hot electrons still heat the target. However, their effects are significantly reduced. Expansion of the Titanium layer is clearly less significant, and the shock is slower. The maximum pressure in the target has also been reduced to ~51 Mbar. This can also be observed in the pressure and density as a function of time and space (Fig. 11, bottom row). The shock now reaches the Titanium layer at ~2.2 ns. However, similar to the precedent simulation, expansion of the Titanium layer prevents from determining the shock breakout time. Figure 12 presents the numerical SOP image postprocessed from the hydrodynamic simulation, and it shows that the rising of the signal due to the shock breakout arrives later. In the time line-out (Fig. 12, right), the delay between the peak due to hot electrons and the signal due to the shock breakout is 3.1 ± 0.15 ns. Adding 600 ps due to the planar geometry gives 3.7 ± 0.14 ns, which is

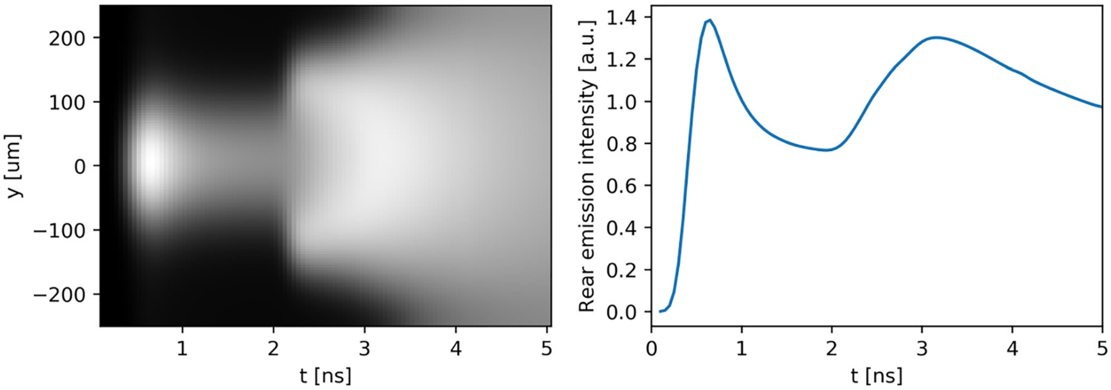

FIG. 10. Synthetic SOP image obtained by postprocessing the results of the CHIC simulation presented in Fig. 9 (left) and line-out of this results along the axis y = 0 (right).

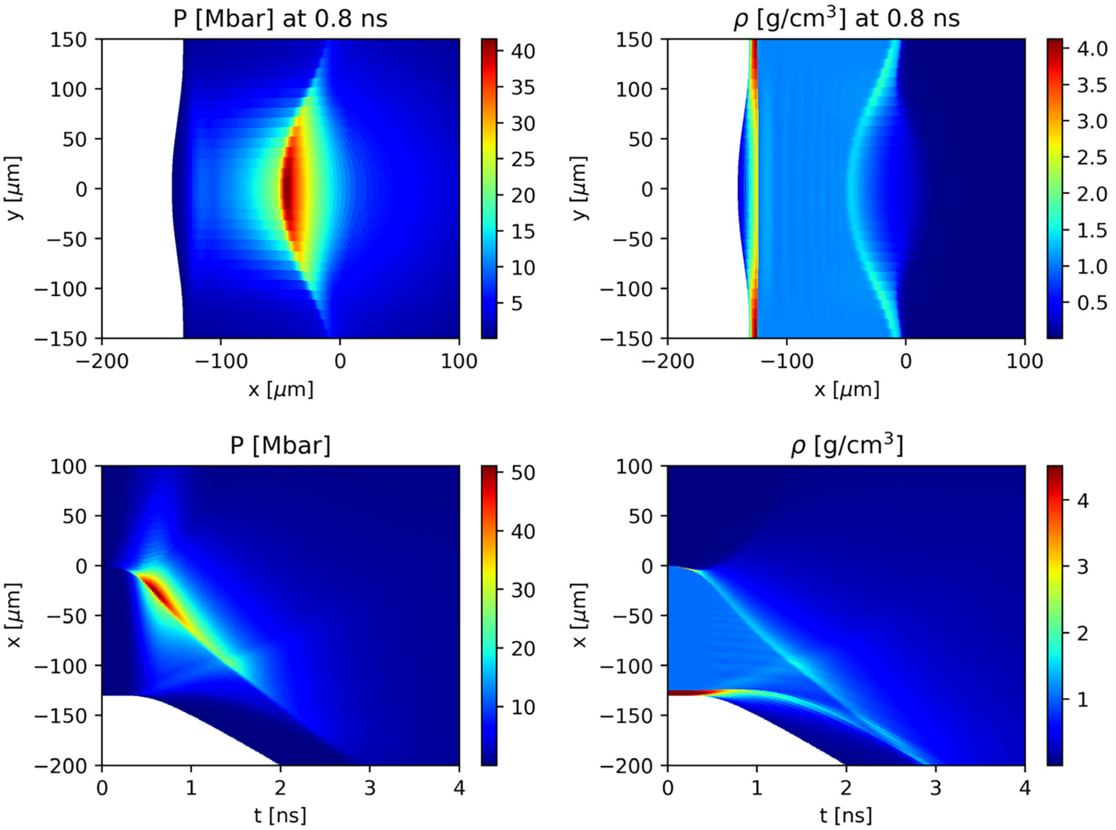

FIG. 11. Simulation with reduced hot electron fluxes. 2D map of pressure at 800 ps (top left). 2D map of density at 800 ps (top right). Pressure as a function of time and space (bottom left). Density as a function of time and space (bottom right).

much closer to the measured delay. Emissivity of the rear side as a function of time and space (Fig. 12, left) shows that the shock breaks out earlier away from the central axis (the earliest being for y $\simeq$ 150 μm). Indeed, expansion of the Titanium layer is more significant near the axis, $y = 0$, and so at this position, the shock propagates a longer distance before breaking out. This effect is also visible in the simulation with the nonreduced fluxes, but in this case, the shock is faster, and therefore, the titanium layer has less time to expand, reducing the difference between the center and the edges of the emission. This effect is not observed in the experimental image, which suggests that in experiment, hot electrons are less directional than what is assumed in the simulation.

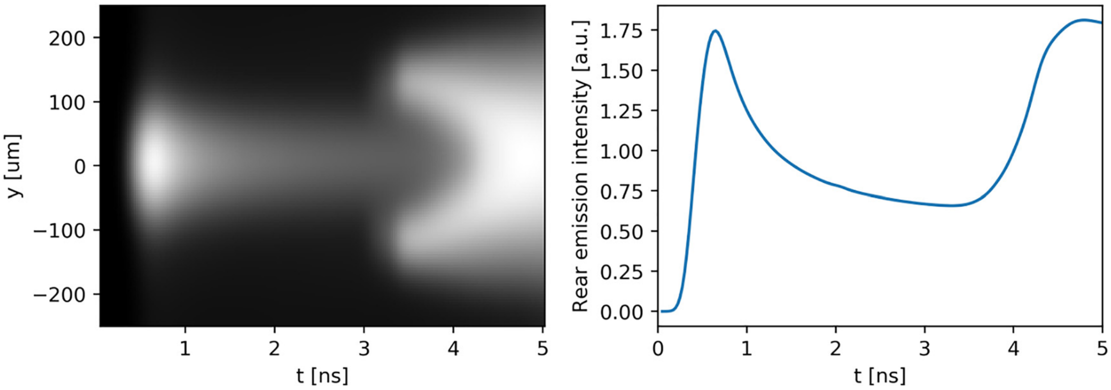

FIG. 12. Synthetic SOP image obtained by postprocessing the results of the CHIC simulation presented in Fig. 11 (left) and line-out of this results along the axis $y = 0$ (right).

I. Effects of angular spreading

We repeated the simulation with reduced fluxes and with ±20° initial divergence for the SRS electron source. While the temperature and conversion efficiency for SRS and TPD hot electrons are kept unchanged, electron heating shown in 2D maps of pressure and density at 0.8 ns, in Fig. 13, is much less directional. This results in a flatter shock front and a decrease in the pressure in both shocked plastic and the corona, the heated volume being larger, for the same injected energy. A lower pressure and cooler unshocked material produces a slower shock. The heated surface zone at the rear side is larger, which reduces the time difference of the shock breakout between the center and edges. Figure 14 shows the numerical SOP image. The curvature of the shock breakout signal is still visible but is strongly reduced. Such a curvature in the experimental image is not apparent but might be blurred due to the low level of the signal. The line-out of the central part of the rear side emission image shows a slightly later shock breakout compared to that in the simulation without initial divergence. The delay between the peak of emission due to hot electrons and the second bump due to the shock breakout is 3.35 ± 0.1 ns. Taking into account 600 ps induced by the planar geometry of simulation leads to a delay of 3.95 ± 0.1 ns, in agreement with the measured delay within error bars. The maximum pressure in the target is now reduced to about 40 Mbar.

The last simulation better reproduces the experimental SOP data, while remaining close to the experimental constraints concerning the measured characteristics of hot electrons. Yet, an increase in the signal due to the shock breakout is steeper in the simulation, and it also starts to decrease after ~4.2 ns. This behavior differs from the experimental signal that slowly increases with time. This difference has already been observed in interpretation of other experiments.[28] Among possible explanations, we mention the equation of state and opacity of Titanium, which might be inaccurate in the regime of low density (below 1 g/cc) and moderate temperature (a few electron volts), induced by rear side expansion.

J. Other plastic thicknesses

Parameters used to reproduce the experimental data for 125 μm targets have also been used to simulate the cases of different plastic thicknesses (50 and 15 μm). Figures 15 and 16 present synthetic SOP images for both cases. The numeric SOP signals are close to the measured ones. For the 50 μm thick CH (Fig. 15, right), the delay between the peak of emission due to hot electrons and the signal due to shock breakout is 1.15 ± 0.10 ns. Adding 50 ps from the planar geometry correction brings this delay in fair agreement with the measured delay (1.0 ± 0.1 ns). Concerning the 15 μm thick CH, the shock breakout does not lead to a significant increase in rear side emissivity. It slightly

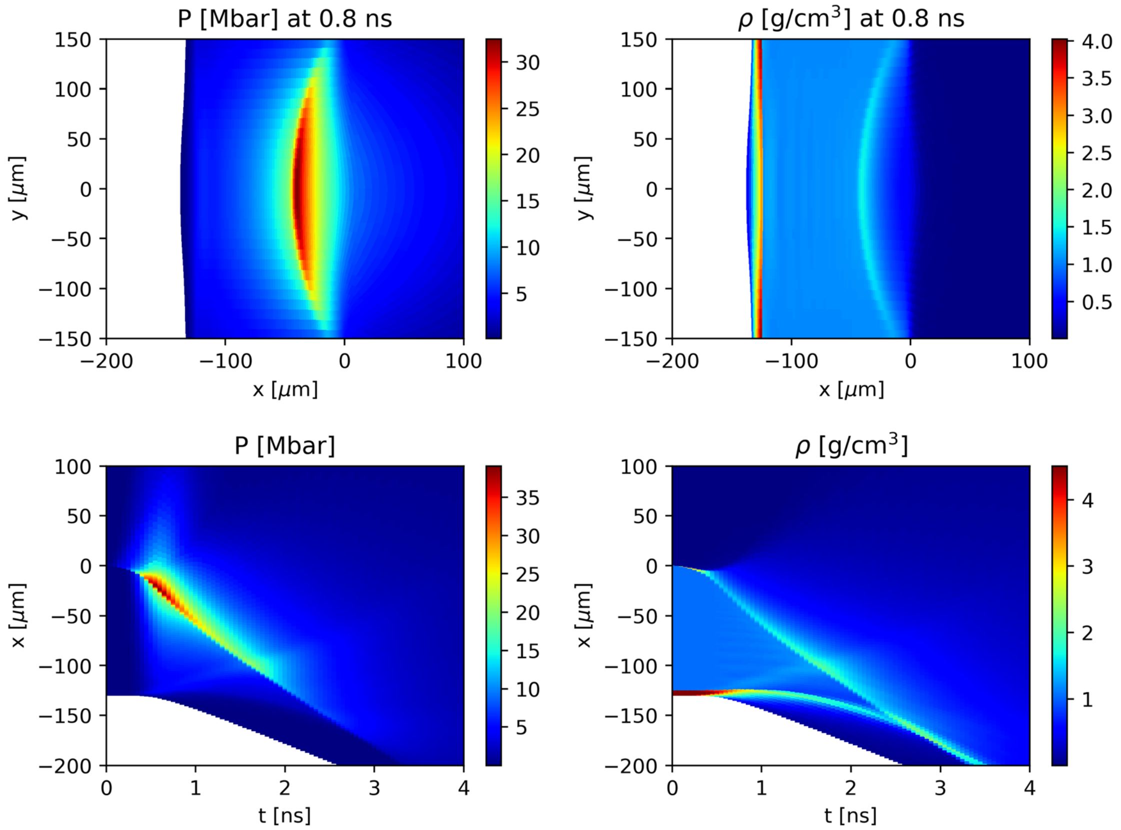

FIG. 13. Simulation with reduced hot electron fluxes and with a ±20° initial divergence of the SRS electron source. 2D map of pressure at 800 ps (top left). 2D map of density at 800 ps (top right). Pressure as a function of time and space (bottom left). Density as a function of time and space (bottom right).

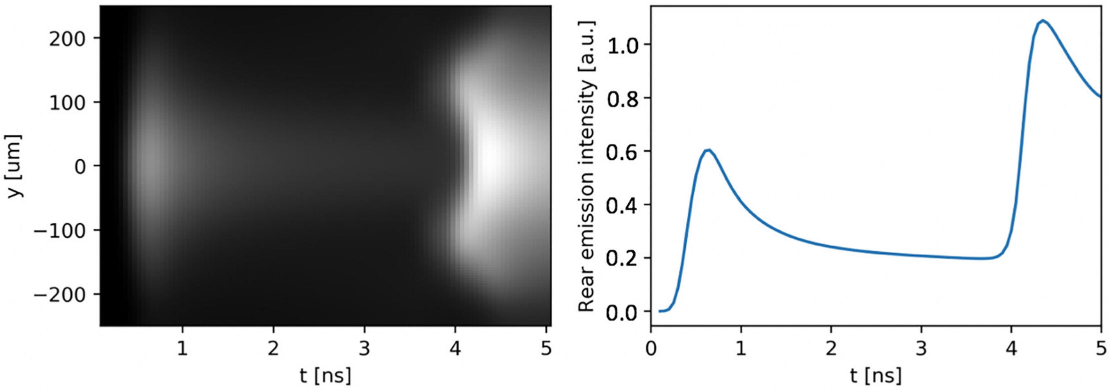

FIG. 14. Synthetic SOP image obtained by postprocessing the results of the CHIC simulation presented in Fig. 13 (left) and line-out of this results along the axis $y = 0$ (right).

changes the slope of the rear side cooling down after being heated by hot electrons. This numerical SOP signal evolution looks similar to the experimental image. Moreover, the overall shape of SOP images and, specifically, the relative brightness of induced-hot electrons and -shock emissions are correctly reproduced. As shock propagates, it compresses and heats matter and loses in strength. So one could expect to obtain a lower emission for the thickest target. This is indeed the case, but heating induced by hot electrons decreases even more rapidly with the thickness. For 15 μm, heating of the Titanium layer exceeds 40 eV during the laser pulse, whereas it is of 28–30 eV and 12–15 eV for target thicknesses of 50 and 125 μm, respectively. This is directly correlated with the electron ranges. The distance of 15 μm of plastic can be crossed by 25 keV electrons, but distances of 50 and 125 μm require energies larger than 50 and 90 keV, respectively. Since hot electron distributions are exponential functions of temperature, the number of electrons at high energy is much smaller, thus reducing the Titanium temperature accordingly. The line-outs presented in Figures 14–16 use the same scale and can be directly compared.

V. CONCLUSION

This work presents experimental results obtained at high intensities and long laser wavelength, $\lambda = 1.315\,\mu$m. These conditions dramatically increase hot electron generation and decrease the role of collisional absorption. A significant fraction of the laser energy absorption is due to parametric instabilities, which are responsible for hot electron generation. Consistent experimental data have been interpreted with the hydrodynamic code CHIC, which accounts for laser-plasma coupling, the generation of hot electrons by SRS and TPD, and their energy depositions. Compared to a previous PALS experiment performed at the short laser wavelength (3ω of the iodine laser), experimental data can be interpreted only if the hot electron parameters are modified. Specifically, the angular spreading of SRS electrons had to be increased, and the hot electron fluxes had to be reduced by a factor between 2 and 4 (depending on whether we consider the threshold for absolute or for convective SRS). Such modifications of the fluxes could be interpreted as the signature of an additional wavelength dependence in the scaling laws for hot electron fluxes. However, they could also be produced by some missing effects in the simulations, eventually enhanced due to the long wavelength used in the experiment: 3D geometry, the presence of a strong magnetic field near the hot electron source, and strong filamentation locally modifying the laser intensity.

Spectroscopic data, data from crystal imagers and from bremsstrahlung cannon, demonstrate the presence of a significant number of hot electrons, a fraction of which can penetrate deeply into the

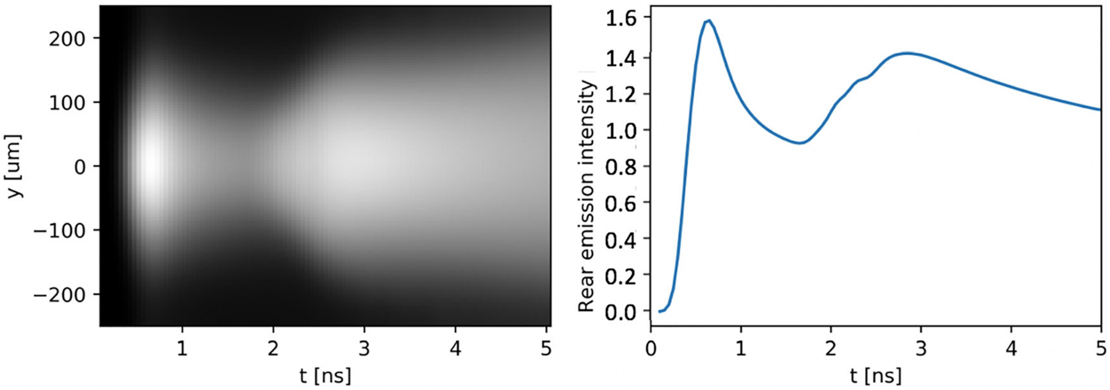

FIG. 15. Synthetic SOP image obtained by postprocessing the results of the CHIC simulation for a 50 μm plastic target (left) and line-out of this results along the axis $y = 0$ (right).

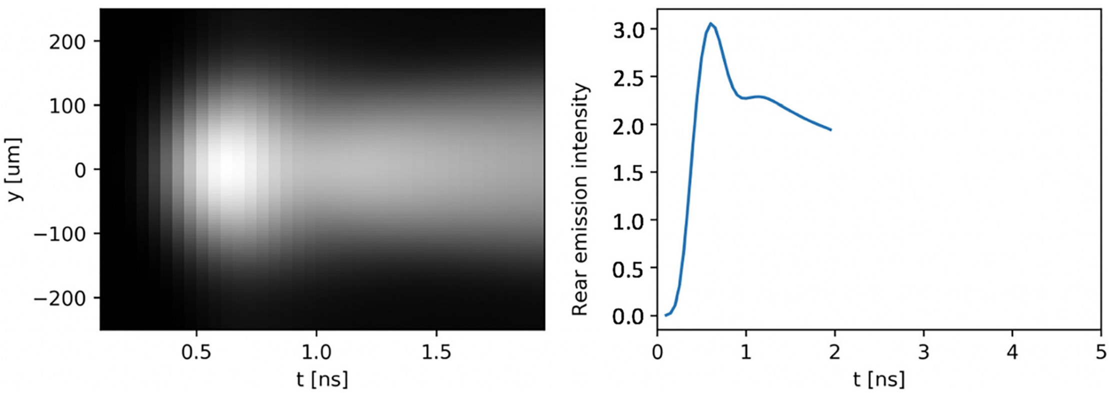

FIG. 16. Synthetic SOP image obtained by postprocessing the results of the CHIC simulation for a 15 μm plastic target (left) and line-out of this results along the axis $y = 0$ (right).

target, suggesting energies beyond 90 keV. Our experimental results and the simulations show a dramatic impact of hot electron preheating on shock dynamics. Energy deposition from hot electrons is clearly visible in the experimental and synthetic SOP images.

Hot electrons strongly increase the shock pressure.[30] The previous experiment performed at PALS, at the third harmonic, showed a pressure increase of 40%.[10] The pressure increase in the present experiment is larger than 250%. This difference comes not only from an enhancement of the hot electron number but also from a weaker laser-mater coupling by collisional absorption. Hot electrons also have a significant impact on shock velocity owing to preheat of the unshocked plastic.

The pressure increase due to hot electrons could be a beneficial factor for shock ignition[29] if one can suppress the strong preheat upstream of the shock front. In our experiment, we used thin targets characterized by a small areal density of $\sim$0.01 g/cm^2, which are unable to stop electrons with energies larger than a few tens of kilo electron volts. In the SI scenario, one should get values of areal density larger than unity for the compressed shell. This could be sufficient to stop all hot electrons downstream of the shock. Therefore, in future shock ignition experiments, hot electrons could turn out to be beneficial for shock amplification, and long wavelength lasers could be a possible alternative for the spike irradiation.

ACKNOWLEDGMENTS

This work was carried out within the framework of the EUROfusion Enabling Research Project: AWP17-ENR-IFE-CEA-01 Preparation and Realization of European Shock Ignition Experiments and received funding from the Euratom Research and Training Program 2014–2018 under Grant Agreement No. 633053. The views and opinions expressed herein do not necessarily reflect those of the European Commission. This work was also supported by the European Union under the Laserlab IV Program (PALS2196); by the Czech Ministry of Education, Youth and Sports, Projects LTT17015, LM2010014, CZ.02.1.01/0.0/0.0/16013/0001552, CZ.02.1.01/0.0/0.0/16013/0001793; and within targeted support of Large Infrastructures, ELI Beamlines Project LQ1606 of the National Program of Sustainability II. Finally, the authors are grateful to the PALS staff for help in running the experiments.

REFERENCES

[1] R. Betti, C. Zhou, K. Anderson, L. Perkins, W. Theobald, and A. Solodov, Phys. Rev. Lett. **98**, 155001 (2007).
[2] R. Craxton, K. Anderson, T. Boehly, V. Goncharov, D. Harding, J. Knauer, R. McCrory, P. McKenty, D. Meyerhofer, J. Myatt *et al.*, Phys. Plasmas **22**, 110501 (2015).
[3] S. Atzeni, X. Ribeyre, G. Schurtz, A. Schmitt, B. Canaud, R. Betti, and L. Perkins, Nucl. fusion **54**, 054008 (2014).
[4] D. Batani, S. Baton, A. Casner, S. Depierreux, M. Hohenberger, O. Klimo, M. Koenig, C. Labaune, X. Ribeyre, C. Rousseaux *et al.*, Nucl. Fusion **54**, 054009 (2014).
[5] W. L. Kruer, *The Physics of Laser Plasma Interactions*, Frontiers in Physics Vol. 73 (Addison-Wesley, 1988)
[6] R. Drake, R. Turner, B. Lasinski, K. Estabrook, E. Campbell, C. Wang, D. Phillion, E. Williams, and W. Kruer, Phys. Rev. Lett. **53**, 1739 (1984).
[7] J. Trela, W. Theobald, K. Anderson, D. Batani, R. Betti, A. Casner, J. Delettrez, J. Frenje, V. Y. Glebov, X. Ribeyre *et al.*, Phys. Plasmas **25**, 052707 (2018).
[8] P. Nicolaï, J.-L. Feugeas, T. Nguyen-Bui, V. Tikhonchuk, L. Antonelli, D. Batani, and Y. Maheut, Phys. Plasmas **22**, 042705 (2015).
[9] D. Batani, L. Antonelli, F. Barbato, G. Boutoux, A. Colaïtis, J.-L. Feugeas, G. Folpini, D. Mancelli, P. Nicolai, J. J. Santos *et al.*, Nucl. Fusion **59**(3), 032012 (2019).
[10] A. Colaïtis, G. Duchateau, X. Ribeyre, Y. Maheut, G. Boutoux, L. Antonelli, P. Nicolaï, D. Batani, and V. Tikhonchuk, Phys. Rev. E **92**, 041101 (2015).
[11] T. Boehly, D. Brown, R. Craxton, R. Keck, J. Knauer, J. Kelly, T. Kessler, S. Kumpan, S. Loucks, S. Letzring *et al.*, Opt. Commun. **133**, 495 (1997).
[12] M. Hohenberger, W. Theobald, S. Hu, K. Anderson, R. Betti, T. Boehly, A. Casner, D. Fratanduono, M. Lafon, D. Meyerhofer *et al.*, Phys. Plasmas **21**, 022702 (2014).
[13] W. Theobald, R. Betti, C. Stoeckl, K. Anderson, J. Delettrez, V. Y. Glebov, V. Goncharov, F. Marshall, D. Maywar, R. McCrory *et al.*, Phys. Plasmas **15**, 056306 (2008).
[14] W. Theobald, R. Nora, M. Lafon, A. Casner, X. Ribeyre, K. Anderson, R. Betti, J. Delettrez, J. Frenje, V. Y. Glebov *et al.*, Phys. Plasmas **19**, 102706 (2012).
[15] R. Nora, W. Theobald, R. Betti, F. Marshall, D. Michel, W. Seka, B. Yaakobi, M. Lafon, C. Stoeckl, J. Delettrez *et al.*, Phys. Rev. Lett. **114**, 045001 (2015).
[16] S. Baton, M. Koenig, E. Brambrink, H. Schlenvoigt, C. Rousseaux, G. Debras, S. Laffite, P. Loiseau, F. Philippe, X. Ribeyre *et al.*, Phys. Rev. Lett. **108**, 195002 (2012).
[17] T. Pisarczyk, S. Gus'kov, O. Renner, N. Demchenko, Z. Kalinowska, T. Chodukowski, M. Rosinski, P. Parys, M. Smid, J. Dostal, J. Badziak, D. Batani, L. Volpe, E. Krousky, H. Turcicova, J. Hrebicek, M. Pfeifer, J. Skala, A. Zaras-Szydlowska, L. Antonelli, Y. Maheut, S. Borodziuk, A. Kasperczuk, and P. Pisarczyk, Laser Part. Beams **33**, 221 (2015).
[18] D. Batani, L. Antonelli, S. Atzeni, J. Badziak, F. Baffigi, T. Chodukowski, F. Consoli, G. Cristoforetti, R. De Angelis, R. Dudzak *et al.*, Phys. Plasmas **21**, 032710 (2014).

[19] K. Jungwirth, A. Cejnarova, L. Juha, B. Kralikova, J. Krasa, E. Krousky, P. Krupickova, L. Laska, K. Masek, T. Mocek *et al.*, Phys. Plasmas **8**, 2495 (2001).
[20] O. Renner, M. Šmíd, D. Batani, and L. Antonelli, Plasma Phys. Controlled Fusion **58**, 075007 (2016).
[21] G. Cristoforetti, A. Colaïtis, L. Antonelli, S. Atzeni, F. Baffigi, D. Batani, F. Barbato, G. Boutoux, R. Dudzak, P. Koester *et al.*, EPL (Europhys. Lett.) **117**, 35001 (2017).
[22] G. Cristoforetti, L. Antonelli, S. Atzeni, F. Baffigi, F. Barbato, D. Batani, G. Boutoux, A. Colaitis, J. Dostal, R. Dudzak *et al.*, Phys. Plasmas **25**, 012702 (2018).
[23] G. Cristoforetti, L. Antonelli, D. Mancelli, S. Atzeni, F. Baffigi, F. Barbato, D. Batani, G. Boutoux, F. D'Amato, J. Dostal, R. Dudzak, E. Filippov, Y. J. Gu, L. Juha, O. Klimo, M. Krus, S. Malko, A. Martynenko, P. Nicolai, V. Ospina, S. Pikuz, O. Renner, J. Santos, V. T. Tikhonchuk, J. Trela, S. Viciani, L. Volpe, S. Weber, and L. A. Gizzi, High Power Laser Sci. Eng. **7**, e51 (2019).
[24] J. Sempau, E. Acosta, J. Baro, J. Fernandez-Varea, and F. Salvat, Nucl. Instrum. Methods Phys. Res. **132**, 377 (1997).
[25] F. Salvat, J. Fernandez-Varea, and J. Sempau, in PENELOPE: A code system for Monte Carlo simulation of electron and photon transport, NEA/NSC/DOC (2015).
[26] J. Breill, S. Galera, and P.-H. Maire, Computers Fluids **46**, 161 (2011).
[27] M. Touati, J.-L. Feugeas, P. Nicolai, J. J. Santos, L. Gremillet, and V. T. Tikhonchuk, New J. Phys. **16**, 073014 (2014).
[28] J. J. Santos, B. Vauzour, M. Touati, L. Gremillet, J.-L. Feugeas, T. Ceccotti, R. Bouillaud, F. Deneuville, V. Floquet, C. Fourment, M. Hadj-Bachir, S. Hulin, A. Morace, P. Nicolai, P. d Oliveira, F. Reau, A. Samake, O. Tcherbakoff, V. T. Tikhonchuk, M. Veltcheva, and D. Batani, New J. Phys. **19**, 103005 (2017).
[29] W. Shang, R. Betti, S. Hu, K. Woo, L. Hao, C. Ren, A. Christopherson, A. Bose, and W. Theobald, Phys. Rev. Lett. **119**, 195001 (2017).
[30] S. Gus'kov, N. Demchenko, A. Kasperczuk, T. Pisarczyk, Z. Kalinowska, T. Chodukowski, O. Renner, M. Smid, E. Krousky, M. Pfeifer, J. Skala, J. Ullschmied, and P. Pizarczyk, Laser and Particle Beams **32**, 177 (2014).